Investigating Ground Effects on Mixing and Afterburning during a TNT Explosion

Ekaterina Fedina & Christer Fureby
The Swedish Defense Research Agency, FOI
Stockholm, Sweden

1 Introduction

The physical complexity of a condensed phase explosions, involving extremely high pressures and temperatures, phase transitions, turbulence, shocks, mixing, instabilities, chemical reactions and deflagration–to–detonation transition puts significant demands on the physical modeling and the numerical simulation techniques. During the early stages of a condensed phase explosion the explosive material is rapidly converted to a hot, dense, high–pressure gas, usually rich in solid carbon, carbon monoxide and hydrocarbons. The explosion products expand at high velocities aiming at pressure equilibrium with the surrounding air, causing a radially expanding supersonic shock wave [1]. Only a small part of the stored chemical energy is released in the detonation process itself. The remaining energy is dissipated more slowly as the detonation products mix with the ambient air and subsequently burn [2]. This afterburning process has little effect on the initial blast wave because it occurs much slower than the original detonation. However, later stages of the blast wave can be affected by the afterburning, particularly for explosions in confined spaces [3], and close to the ground [4].

The main objective of this paper is to gain further understanding of the physical processes involved in a near–ground air blast, from the detonation throughout the afterburning stage. To achieve this we here address and compare two rather fundamental and related situations: (i) the explosion of a charge in free air and (ii) the explosion of a charge in close proximity of the ground. The simulation results will be used to investigate and elucidate the physical processes associated with the rapidly evolving shock wave and the much more slowly evolving mixing and afterburning processes and what effect the vicinity of the ground has on these processes. The goal is to capture the significant stages of turbulent mixing, involving the initial blast wave, secondary shock, implosion and the constant mixing stages, providing further knowledge of the complicated processes during a condense phase explosion event, thereby shedding further light on how mixing and the subsequent afterburning are behaving with and without confinement.

2 LES Modeling of Combustion

The reactive flow equations are balance equations of mass, momentum and energy describing the convection, diffusion and reactions. In this study we adopt an LES model [5], where the filtered mass, momentum, energy and species equations, in the absence of body forces, are:

$$\begin{aligned}
&\partial_t(\bar{\rho}) + \nabla\cdot(\bar{\rho}\tilde{\mathbf{u}}) = 0,\\
&\partial_t(\bar{\rho}\tilde{\mathbf{u}}) + \nabla\cdot(\bar{\rho}\tilde{\mathbf{u}}\tilde{\mathbf{u}}) = -\nabla\bar{p} + \nabla\cdot\left(\left((\beta-\tfrac{2}{3}\mu)\nabla\cdot\tilde{\mathbf{u}}\delta_{ij} + 2\mu\tilde{\mathbf{D}}\right) - \mathbf{B}\right)\\
&\partial_t(\bar{\rho}\tilde{h}) + \nabla\cdot(\bar{\rho}\tilde{h}\tilde{\mathbf{u}}) = -\dot{\bar{p}} + \left((\beta-\tfrac{2}{3}\mu)\nabla\cdot\tilde{\mathbf{u}}\delta_{ij} + 2\mu\tilde{\mathbf{D}}\right)\cdot\nabla\tilde{\mathbf{u}} + \nabla\cdot\left(\kappa\nabla\tilde{T} - \mathbf{b}_h\right)\\
&\partial_t(\bar{\rho}\tilde{Y}_i) + \nabla\cdot(\bar{\rho}\tilde{\mathbf{u}}\tilde{Y}_i) = \nabla\cdot\left(\tfrac{\mu}{Sc_i}\nabla\tilde{Y}_i - \mathbf{b}_i\right) + \overline{\dot{w}}_i.
\end{aligned} \tag{1}$$

Correspondence to: ekaterina.fedina@foi.se

Here $\bar{\rho}$ is the density, $\tilde{\mathbf{u}}$ the velocity, $\bar{p}$ the pressure, $\tilde{h}$ the enthalpy, $\tilde{T}$ the temperature, $\tilde{\mathbf{D}}$ the symmetric part of $\nabla\tilde{\mathbf{u}}$, $\overline{\dot{w}_i}$ the reaction rate and $\tilde{Y}_i = \bar{\rho}_i/\bar{\rho}$ the mass fraction of species i, $\mathbf{B}$, $\mathbf{b}_h$ and $\mathbf{b}_i$ are the unresolved subgrid stress tensor and flux vectors, respectively. Moreover, β is the bulk viscosity, μ the shear viscosity, while κ is the thermal conductivity, $Sc_i = \frac{\mu_i}{\bar{\rho}D_i}$ is the Schmidt number and D_i the diffusivity of the species i, respectively. We adopt the conventional caloric Equation Of State (EOS), $\tilde{h} = \sum_i^N (\tilde{Y}_i h_{f,i}^\theta) + \sum_i^N \left(\tilde{Y}_i \int_{T_0}^T c_{p,i} dT\right)$ in which $h_{f,i}^\theta$ is the enthalpy of formation at STP for the species i, $c_{p,i}$ is the specific heat at constant pressure for species i and T_0 is the ambient temperature of the surrounding. Here, $c_{p,i}$ are assumed to be linear functions of T. The thermal EOS is a Nobel–Abel EOS, following [6, 7], in which $p = \frac{\rho R_0 \sum_i (Y_i/M_i) T}{1 - An}$, where A is an empirical constant that accounts for the co–volume where reactions take place, n is the number of moles per unit volume, with molar mass M_i and the universal gas constant R_0. In the simulations presented here we use a combination of ideal gas law for the air and burned gases and Nobel–Abel EOS for the detonation products. To close the filtered LES equations, Eq. 1, we utilize a functional model approach for the subgrid stress tensor and flux vectors, formulating $\mathbf{B} \approx -\mu_k \tilde{\mathbf{D}}$, $\mathbf{b}_h \approx (\frac{\mu_k}{Pr_k})\nabla\tilde{h}$ and $\mathbf{b}_Y \approx (\frac{\mu_k}{Sc_k})\nabla\tilde{Y}_i$ in which Pr_k is the turbulent Prandlt number, Sc_k is the turbulent Schmidt number and μ_k is the turbulent subgrid density to be modeled. Following Cook & Cabot we here adopt a hyperviscosity model [8] due to its documented ability to capture the fine vorticity structures that arise during the afterburning process.

In the simulations we employ a reduced TNT mechanism developed by Tran, [9], implemented here as a three–step mechanism for the TNT combustion:

$$\begin{array}{lrcl} (1) & C_7H_5N_3O_6 & \rightarrow & 1.5N_2 + 2.5H_2O + 3.5CO + 3.5C \\ (2) & C + \frac{1}{2}O_2 & \rightarrow & CO \\ (3) & CO + \frac{1}{2}O_2 & \rightarrow & CO_2 \end{array}$$

in which the first step represents the initial decompositions of TNT and the latter reaction steps represent the afterburn process. The reaction rates are assumed to be of Arrhenius form $\dot{w}_i = M_i \sum_{i=1}^N P_{ij}\dot{w}_j$ with $\dot{w}_j = A_j e^{(-T_{a_j}/T)} \prod_{i=1}^N (\bar{\rho}\tilde{Y}_i)^{P'_{ij}}$, considering only the forward reactions, in which M_i is the molar mass of species i, P_{ij} the stoichiometric coefficients, $\dot{w}_j$ the reaction rate of j^{th} reaction step. Moreover, A is the Arrhenius pre–exponential factor and T_a the activation temperature. The low-pass filtered reaction rates, $\overline{\dot{w}_i}$ from Eq. 1, are modeled using the Partially Stirred Reactor (PaSR) model [10]. The PaSR is a Finite Rate Chemistry (FRC) [11] model based on the conjecture that any turbulent flow can be divided into fine structures $(*)$ and surroundings $(^0)$. Since most of the mixing occurs in the fine structures, the reactions also take place there as the reactants are mixed at scales down to the molecular scales. This implies that the filtered reaction rates can be modeled as $\overline{\dot{w}_i(\bar{\rho}, \tilde{Y}_i, \tilde{T})} = \gamma^* \dot{w}_i(\bar{\rho}, Y_i^*, T^*)$ in which γ^* is the reacting subgrid volume fraction. For the details on modeling of γ^* we refer to [11].

The LES equations are discretized using Reynolds transport theorem in a finite volume framework, designed to handle arbitrary cell–shapes, utilizing the OpenFOAM library [12]. The code uses an unstructured collocated Finite Volume (FV) method [12], in which the discretization is based on Gauss theorem together with an explicit time–integration scheme, which is performed by a second order accurate TVD Runge–Kutta scheme [13]. The equations are solved with full coupling between the equations with a fixed time step corresponding to a Courant number of about 0.02.

3 Simulation Setup

A spherical, 1.42 kg, TNT charge with a radius of 6 cm is here computationally detonated in unconfined and semi-confined air. The unconfined detonation simulation is performed in a cubic domain of size $5 \times 5 \times 5$ m^3, whereas the semi–confined detonation simulation is performed in a rectangular domain of size $5 \times 5 \times 3.56$ m^3, yielding computational grids of 32 and 24 Mcells, respectively. In the unconfined case the detonation product cloud was initiated at the center of the cube, while in the semi–confined case the fireball was placed 0.5 m above ground to facilitate shock reflection patterns. In the free air case, all boundary conditions were Neumann conditions, while in the semi–confined case the ground was modeled by a no–slip boundary condition and a constant temperature of 298 K while all other boundary conditions were Neumanns conditions.

The initial conditions, representing the explosive decomposition and the formation of the initial cloud of hot detonation products at high temperature (the fire ball), are obtained from Balakrishnan & Menon [14] and consist of one–dimensional (1D) profiles, of velocity, pressure, density as well as temperature and stoichiometric species

compositions from the first reaction spherically mapped onto the 3D grid. This spherically symmetric cloud is then perturbed by a small random perturbation to facilitate the development of various types of instabilities. The unburned air is set to have atmospheric pressure and temperature, as well as the air concentration mass fractions oxygen and nitrogen of 0.23/0.77 respectively. These simulation results have been validated against experiments with good agreement, in [15].

4 Results and Discussion

Figure 1 shows an overview of the simulation results in terms of the pressure gradient, $\nabla\bar{p}$, chosen to show the propagation of the shock waves and the mass fraction of carbon dioxide, $\tilde{Y}_{CO_2}$, which visualizes the mixing and the afterburning. In Fig. 1a the key features of an unconfined explosion are revealed. The outgoing blast wave (white rings in the pressure gradient distribution of Fig. 1a) heats up and accelerates the ambient air as it propagates through it. Early in the process (seen here at 0.5 ms) a rarefaction wave (dark blue region in $\nabla\bar{p}$ distribution) propagates inwards, boosting the acceleration caused by the blast wave, and later forcing an outward directed acceleration of the hot detonation gases. As seen in the distribution of $\tilde{Y}_{CO_2}$ in Fig. 1a at times 0.5 ms and 1 ms, the interface between the detonation products and the shock–compressed air is impulsively accelerated, resulting in the development of Rayleigh–Taylor (RT) instabilities, [16]. The results suggest that a short time after the initial blast the ingoing rarefaction wave will overexpand the flow causing a secondary shock (light blue), resulting in the formation of a thin mixing layer, initially seen at 0.5 ms in $\tilde{Y}_{CO_2}$ distribution, between the initial blast wave and the secondary shock. The secondary shock will eventually strengthen by means of detonation product gases accelerating it, and subsequently further strengthening to the point of implosion (seen at 1.5 ms). The implosion will entrain the air into the mixing layer, enhancing the afterburning (seen at 1 ms and 1.5 ms in $\tilde{Y}_{CO_2}$). When the secondary shock reflect from the origin (at 1.5 ms) it is redirected outwards (at 2.0 ms) to interact with the existing RT instabilities, depositing additional vorticity into the mixing layer due to baroclinic effects, giving rise to Richtmyer–Meshkov (RM) instabilities, [17]. This further enhances the turbulent mixing (at 2.0 ms in $\tilde{Y}_{CO_2}$ distribution). At the later stages (from 2–3 ms in Fig. 1a) the remaining fuel is consumed in the core of the blast in an almost constant–pressure mixing layer.

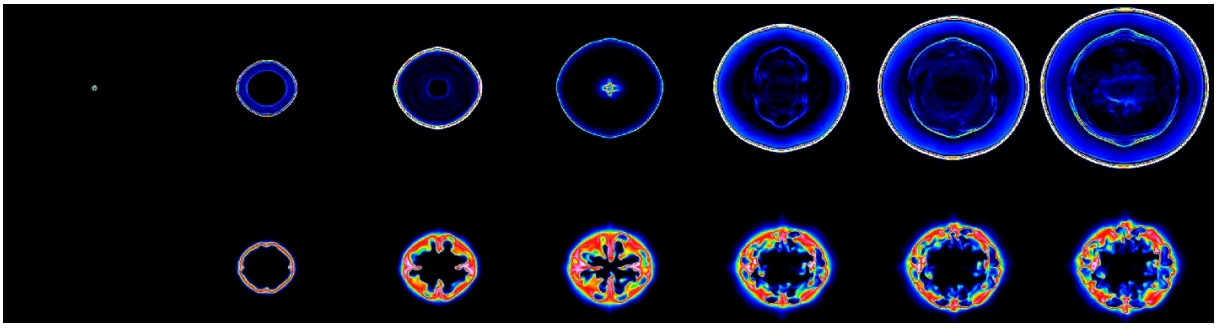

(a) Free air

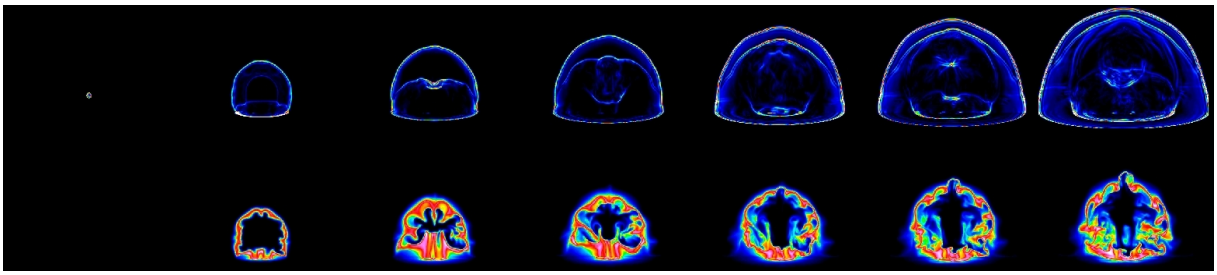

(b) Near ground

Figure 1: Time series of the explosion event, featuring from the top down: $|\nabla\bar{p}|$ and $\tilde{Y}_{CO_2}$. The times are, from left to right: 0 ms, 0.5 ms, 1 ms, 1.5 ms, 2 ms, 2.5 ms and 3 ms.

Figure 1b illustrates the results of the semi–confined TNT explosion. The initial blast wave expands outwards in the air as well as parallel to the ground. After the blast wave is reflected by the ground (at 0.5 ms) it propagates inwards, initially as two separate shock waves, into the mixing layer, creating behind it a low pressure region that entrains air into the combustion zone. This effect is seen as a mushroom shaped fireball, visible e.g. in the $\tilde{Y}_{CO_2}$ distribution at 1.0 ms. The ground reflected shocks collide (at 1.0 ms) with an ingoing rarefraction wave (origin of which is seen in Fig. 1b at 0.5 ms) forming a complex mixing zone around the collision point (seen in $\nabla\bar{p}$), and two new shocks are formed, one propagating upwards and one downwards towards the ground. These shock systems form strong up– and downwashes of the detonation products that enhances the mixing (development seen from 1.0 ms to 2.0 ms in $\nabla\bar{p}$ distribution). Even here the RT instabilities are created between in the burning interface and the propagation of the ground reflected shock upwards gives rise to the misaligned pressure and density gradients, creating RM instabilities. In the later stages, time 2.5 ms and 3 ms new shock systems arise and collide, mach stems are also visible under the last three times.

Figure 2a further elucidates the mixing properties of both cases. Here the mixing is illustrated through a mixing layer thickness, δ, defined as $\delta/R_0(t) = \left(\overline{R_{0.1}}(t) - \overline{R_{0.9}}(t)\right)/R_0$, [1], where $\overline{R_{0.1}}$ is the average radius where the mass fraction of carbon is $\tilde{Y}_C = 0.1Y_{C,max}$, $\overline{R_{0.9}}$ follows as an average radius where $\tilde{Y}_C = 0.9Y_{C,max}$ and $R_0 = 0.06$ m is the initial blast radius. In the free air case a continuous increase of the δ is observed. After a short expansion phase (∼0–0.1 ms), as the rarefaction wave starts propagating inwards, δ grows linearly due to the generation of RT instabilities that initiate the mixing layer by means of vorticity, this is also visible in Fig. 2b as the separation of $\overline{R_{0.1}}$ and $\overline{R_{0.9}}$ lines. Before the implosion, seen best in Fig. 2b as $\overline{R_{0.9}}$ dips at 1.2 ms, the δ growth stagnates briefly and resumes to climb after the implosion as new air is deposited into the mixing layer. The growth slowly subsides until the reflected shock passes through the mixing layer (∼2.1–2.5 ms) depositing more vorticity by means of RM instabilities. The mixing layer thickness then continues to expand by means of volumetric expansion due to heat release from the afterburning, as a decline of $\overline{R_{0.9}}$ in Fig. 2b indicates an increase in the fuel consumption. The δ profile of the semi–confined case confirms the pulsation of the shock systems, arising and decaying by means of interaction with the ground. The mixing layer is initially expanding, with a slightly larger δ compared to the unconfined case, which is attributed to the low pressure regions behind the ground reflected shocks that entrain air into the mixing layer. Instead of implosion, the δ profile shows a contraction of the mixing layer between 1 ms and 1.5 ms, which is caused by the collision of the ground reflected shocks and an inward propagating rarefaction wave, followed by entrainment of air into the mixing layer and the generation of RM instabilities. While in the free air case δ grows continually, the near ground scenario shows a second decline in the profile, from 2.2 ms. This is yet again caused by a collision of the shock waves (seen in Fig. 1b at 2.5 ms and 3 ms) compacting the mixing layer. In this simulation, the volume of the domain restricted the propagation of the shock waves system, have the domain been larger, a sigmoidal profile would have emerged for the near ground mixing thickness. This implies that the vicinity of the ground, enables generation of a complex shock pattern, due to the ground reflection, enforcing shock wave interaction, which in turn creates new shock wave systems that propagate both upwards and downwards, subsequently colliding. These complex propagation patterns maintain the mixing layer, inhibiting the stagnation of its growth. This also indicates that in this scenario the mixing and thereby the afterburning are prolonged in time and the performance of an explosive compound regarding these effects is increase if detonated in the vicinity of an obstacle.

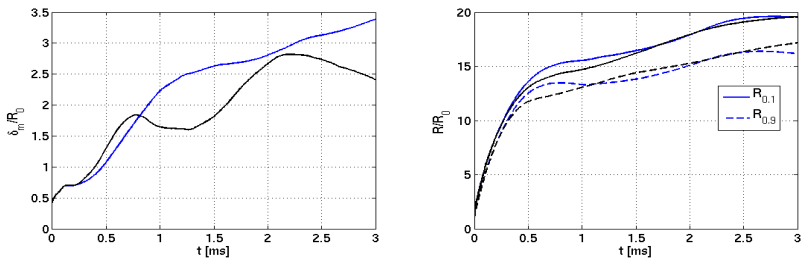

(a) (b)

Figure 2: Mixing layer evolution featuring (a) mixing layer thickness, (b) $\overline{R_{0.1}}$ and $\overline{R_{0.9}}$. Legend: (—) unconfined case, (—) semi–confined case.

To relate mixing and afterburning processes we investigate in detail the vorticity $\tilde{\omega} = \frac{1}{2}\nabla \times \tilde{\mathbf{u}}$, baroclinic production term $(\nabla\bar{\rho} \times \nabla\bar{p})/\bar{\rho}^2$, heat release $\dot{Q} = \sum_i \left(M_i P_{ij} \overline{\dot{w}}_i h^{\theta}_{f,i}\right)$ and kinetic energy $\frac{1}{2}\tilde{\mathbf{u}}^2$ over the surface of $R_{0.1}$, that is, over the iso–surface of $\tilde{Y}_C = 0.1Y_{C,max}$. These quantities are integrated over $R_{0.1}$ for each time step and the results are presented in Fig. 3a for times 1.25–2.5 ms. The figure shows $(\nabla\bar{\rho} \times \nabla\bar{p})/\bar{\rho}^2$, $|\tilde{\omega}|$, $\frac{1}{2}\tilde{\mathbf{u}}^2$ and $\dot{Q}$ normalized with various factors of 10 to fit into a single graph, featuring a passage of the reflected shock systems through the $R_{0.1}$ and their ripple effects on the mixing and afterburning. Between 1.5 ms and 2 ms a shock system of an upward and a downward directed shocks propagates through the iso–surface of $\tilde{Y}_C = 0.1Y_{C,max}$ generating vorticity, seen as spikes at 1.65 ms and 1.75 ms in Fig. 3a, which in turn gives rise the heat release peak at 1.71 ms due to enhanced convective mixing attributed to the vorticity production. After 2ms (seen in Fig. 1b) the shocks revers and are now traveling towards each other as they pass through the $\tilde{Y}_C$ iso–surface, yet again depositing vorticity which increases heat release at 2.17 ms.

In Fig. 3b we present a detailed view of these processes by means of the iso–surface of $\tilde{Y}_C = 0.1Y_{C,max}$ colored by temperature and combined with pink iso–surface of vorticity at three time instances; 1.71 ms, 2 ms and 2.17 ms. By studying Fig. 3b an increase in both the temperature and vorticity is obvious between the time instances, the heat release also causes a volumetric expansion which in turn widens the vortical structures, whereas the baroclinic production term, caused by the misalignment between the density and pressure gradients, generates vorticity, as seen in Fig. 3a. The vorticity is visibly wrapped around the instability structures fragmenting the fuel iso–surface and it is clearly shown that the hottest regions are located along the vorticity structures, where the afterburning takes place. Both Fig. 3a and b indicate that the heat release occurs in topologically fragmented structures surrounding the fuel distribution that still dominates the core of the detonation. The rate of heat release is controlled by the convective mixing of fuel and air from either side of the heat release zone, making the combustion process behave similar to a highly turbulent diffusion flame.

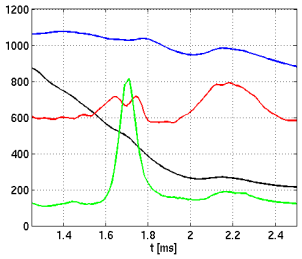

(a)

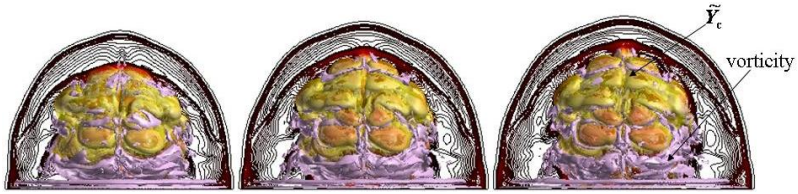

(b)

Figure 3: (a) Normalized (—) baroclinic production term, (—) vorticity, (—) kinetic energy and (—) heat release integrated over the iso–surface of $\tilde{Y}_C = 0.1Y_{C,max}$. (b) Contour lines of kinetic energy with the iso–surface of $\tilde{Y}_C = 0.1Y_{C,max}$ colored by temperature and iso–surface of vorticity (in pink) at 1.71 ms, 2.0 ms, 2.17 ms (left to right).

5 Conclusions

Combustion and mixing behind an blast wave have been investigated for TNT condense phase explosions in free air and in the vicinity of the ground using a LES–PaSR finite rate chemistry model. RT instabilities generated during explosion event gave rise to vorticity and mixing, where the vorticity was found to be formed by exothermicity due to misaligned pressure and density gradients. The analysis also indicated that the heat release and thereby combustion take place around the vorticity filaments, hence predicting afterburning and mixing behind a blast wave. The near surface explosions showed that the patterns and features involved in mixing and combustion are fundamentally the same as for the free air detonation. The vicinity to the ground affects the pressure magnitude and alters the shock propagation pattern, which affects the mixing layer and gives the combustion region a mushroom shape, however the heat release is still oriented around the vorticity structures. The almost sigmoidal shape of the mixing layer thickness profile indicates that even though both cases exhibited the same flow and combustion dynamics, the effect of the ground creates complex shock systems which ultimately increase the performance of an explosive charge by prolonging the existence of the mixing layer and thereby the afterburning due to pulsating behavior of the shock wave systems caused by semi–confinement.

Acknowledgments

This work was sponsored by the Swedish Armed Forces.

References

[1] J. R. Bowen, Ed., *Dynamics of Exothermicity*. Gordon and Breach Publishers, 1992, chapter 13, Spherical Mixing Layers in Explosions.

[2] A. Kuhl, R. Fergusson, and A. Oppenheim, "Gasdynamic model of turbulent exothermic fields in explosions," *Progress in Astronautics and Aeronautics*, vol. 173, pp. 251–261, 1963.

[3] W. Ingignoli, "Etude de la formation et de la propagation des detonations dans des suspensions de particules d'aluminium en atmosphere oxydante ou reactive," Ph.D. dissertation, Universit de Poitiers, 1999.

[4] H. Almström, "Registration and simulation of air blast pressure of a detonation charge above ground," Swedish Defence Research Agency, Weapons and Protection Division, Methodology Report FOI-R–0819–SE, 2003.

[5] C. Fureby, "Towards large eddy simulation in engineering," *Prog. Aerospace Science*, vol. 44, p. 381, 2008.

[6] I. Johnston, "The noble–abel equation of state: Thermodynamic derivations for ballistic modeling," Australian Government Department of Defence, Defence Science and Technology Organisation, Tech. Rep. DSTO-TN-0670, 2005.

[7] C.-K. Kim, J. Moon, J.-S. Hwang, M.-C. Lai, and K.-S. Im, "Afterburning of tnt explosive products in air with aluminum particles," *46th AIAA Aerospace Sciences Meeting*, 2008.

[8] A. Cook and W. Cabot, "Hyperviscosity for shock–turbulence interactions," *J. Comp. Phys.*, vol. 203, p. 379, 2005.

[9] T. Tran, R. Simpson, J. Maienschein, and C. Tarver, *32nd International Conference of Institute of Chemistry Technology*, 2001.

[10] E. Baudoin, K. Nogenmyr, X. Bai, and C. Fureby, "Comparison of les models applied to a bluff body stabilized flame," *AIAA 2009-1178*, 2009.

[11] M. Berglund, E. Fedina, C. Fureby, J. Tegner, and V. Sabel'nikov, "Finite rate chemistry large–eddy simulation of self–ignition in a supersonic combustion ramjet," *AIAA Journal*, vol. 48, pp. 540–550, 2010.

[12] H. Weller, G. Tabor, H. Jasak, and C. Fureby, "A tensorial approach to cfd using object oriented techniques," *Comp. in Physics*, vol. 12, p. 629, 1997.

[13] S. Gottlieb and C.-W. Shu, "Total variation diminishing runge–kutta schemes," *Mathematics of Computation*, vol. 67, p. 73, 1998.

[14] K. Balakrishnan and S. Menon, "A numerical investigation of shear instability, mixing and afterburn behind explosive blast waves," *47th AIAA Aerospace Sciences Meeting, January 5–8*, 2009.

[15] E. Fedina, C. Fureby, and A. Helte, "Predicting mixing and combustion in the afterburn stage of air blasts," *AIAA–2010-0773*, 2010.

[16] G. Taylor, "The instability of liquid surfaces when accelerated in a direction perpendicular to their planes," *Proc. of Royal Society of London. Series A*, vol. 201, p. 192, 1950.

[17] R. Richtmyer, "Taylor instability in a shock acceleration of compressible fluids," *Com. Pure and Appl. Math.*, vol. 13, p. 297, 1960.